PHYSICAL REVIEW E **88**, 060403(R) (2013)

Instabilities at frictional interfaces: Creep patches, nucleation, and rupture fronts

Yohai Bar-Sinai,[1] Robert Spatschek,[2] Efim A. Brener,[1,3] and Eran Bouchbinder[1]
[1]*Chemical Physics Department, Weizmann Institute of Science, Rehovot 76100, Israel*
[2]*Max-Planck-Institut für Eisenforschung GmbH, D-40237 Düsseldorf, Germany*
[3]*Peter Grünberg Institut, Forschungszentrum Jülich, D-52425 Jülich, Germany*
(Received 16 June 2013; published 10 December 2013; corrected 20 December 2013)

The strength and stability of frictional interfaces, ranging from tribological systems to earthquake faults, are intimately related to the underlying spatially extended dynamics. Here we provide a comprehensive theoretical account, both analytic and numeric, of spatiotemporal interfacial dynamics in a realistic rate-and-state friction model, featuring both velocity-weakening and velocity-strengthening behaviors. Slowly extending, loading-rate-dependent creep patches undergo a linear instability at a critical nucleation size, which is nearly independent of interfacial history, initial stress conditions, and velocity-strengthening friction. Nonlinear propagating rupture fronts—the outcome of instability—depend sensitively on the stress state and velocity-strengthening friction. Rupture fronts span a wide range of propagation velocities and are related to steady-state-front solutions.

DOI: 10.1103/PhysRevE.88.060403 PACS number(s): 46.50.+a, 62.20.Qp, 46.32.+x, 91.55.Fg

Introduction. Predicting the strength and stability of frictional interfaces is an outstanding problem, relevant to a broad range of fields—from biology and nanomechanics to geophysics. Recent modeling efforts [1–20] and novel laboratory experiments [21–32] have revealed complex spatiotemporal dynamics that precede and accompany interfacial failure. In particular, frictional instabilities that mark the transition from creep-like motion to rapid slip and a variety of emerging rupture fronts have been observed. Quantitatively understanding these complex dynamics and their dependence on geometry, external forcing, system history, and constitutive behavior of the frictional interface remains an important challenge.

In this Rapid Communication we theoretically study a simple, yet realistic, quasi-1D rate-and-state model [33,34] in which friction is velocity-weakening at low slip velocities and crosses over to velocity-strengthening at higher velocities [35–37]. Using combined analytic and numeric tools we elucidate the physics of a sequence of instabilities at a frictional interface. In particular, we study the dynamics of slowly extending creep patches [38–40], their stability, and the emerging nonlinearly propagating rupture fronts.

The model. The friction model we study is the realistic rate-and-state model introduced in [37], which is briefly presented here. The spatially extended interface between two dry macroscopic bodies is composed of an ensemble of contact asperities whose total area A_r is much smaller than the nominal contact area A_n [41]. The normalized real contact area, $A \equiv A_r/A_n \ll 1$, is given as $A(\phi) = [1 + b\ln(1 + \phi/\phi^*)]\,\sigma/\sigma_H$, where ϕ is a state variable quantifying the typical time passed since the contact was formed (i.e., its "age"). σ is the normal stress, σ_H is the hardness, b is a dimensionless material parameter, and ϕ^* is a short time cutoff [24,29]. The frictional resistance stress τ is decomposed as $\tau = \tau^{\rm el} + \tau^{\rm vis}$, where $\tau^{\rm el}$ is related to elastic deformation of the contact asperities and $\tau^{\rm vis}$ to their rheological response. The latter is related to thermally activated processes and is given by $\tau^{\rm vis}(v,\phi) = \eta\, v^* A(\phi)\ln(1 + v/v^*)$ [5,42,43], where v is the slip velocity, η is a viscous-friction coefficient, and v^* is a small velocity scale.

The dynamic evolution equations for the friction variables take the form [5,34,37]

$$\dot{\phi} = 1 - |v|\frac{\phi}{D}\,g(\tau,v),$$
$$\dot{\tau}^{\rm el} = \frac{\mu_0}{h}A(\phi)v - |v|\frac{\tau^{\rm el}}{D}\,g(\tau,v). \tag{1}$$

Here D is a characteristic slip distance, μ_0 is the interfacial elastic modulus, and h is the effective height of the interface. To understand the role of $g(\tau,v)$, first set it to zero. Then, the equations yield $\phi = t$, which corresponds to the well-established logarithmic aging of $A(t)$, and an elasticity relation $\tau^{\rm el} \simeq \mu_0 A(t)u/h$ [where $A(t)$ varies much slower than the elastic response and u is the slip displacement; recall that $\dot{u} = v$]. These relations describe the response of the interface in the absence of irreversible slip. When $g(\tau,v) = 1$, the second terms on the right-hand side of Eqs. (1) describe the breakage of contact asperities accompanied by irreversible slip over a length D on a time scale D/v. Therefore, $g(\tau,v)$ plays the role of an effective threshold for the onset of irreversible slip. In [37], $g(\tau,v)$ described a sharp threshold in terms of the stress τ. Here, we choose $g(\tau,v) \equiv \sqrt{1 + v_0^2/v^2}$, with an extremely small $v_0 = 10^{-9}$ m/s. Thus, $|v|\,g(\tau,v)$ changes from v_0 for $v \to 0$ to $|v|$ for $v \gg v_0$. Our results are insensitive to this choice of $g(\tau,v)$.

Consider a rigid substrate and a long elastic body (in the x direction) of height H (in the y direction) pressed against it by a constant normal stress σ applied at $y = H$; see Fig. 1(a). The friction law formulated above describes the interface at $y = 0$. The elastic body is described by Hooke's law and its force balance equation, in the limit of small H, reads

$$\rho H\ddot{u} = \bar{G}(\nu)H\partial_{xx}u - \tau, \tag{2}$$

where ρ is the mass density and $\bar{G}(\nu)$ is an effective elastic modulus depending on Poisson's ratio ν and proportional to the shear modulus G [44]. In this quasi-1D approximation, σ is space- and time-independent.

The material parameters we use below were extracted from extensive experimental data of PMMA. We set $D = 0.5\ \mu$m and the rest of the parameters appear in [44]. The steady

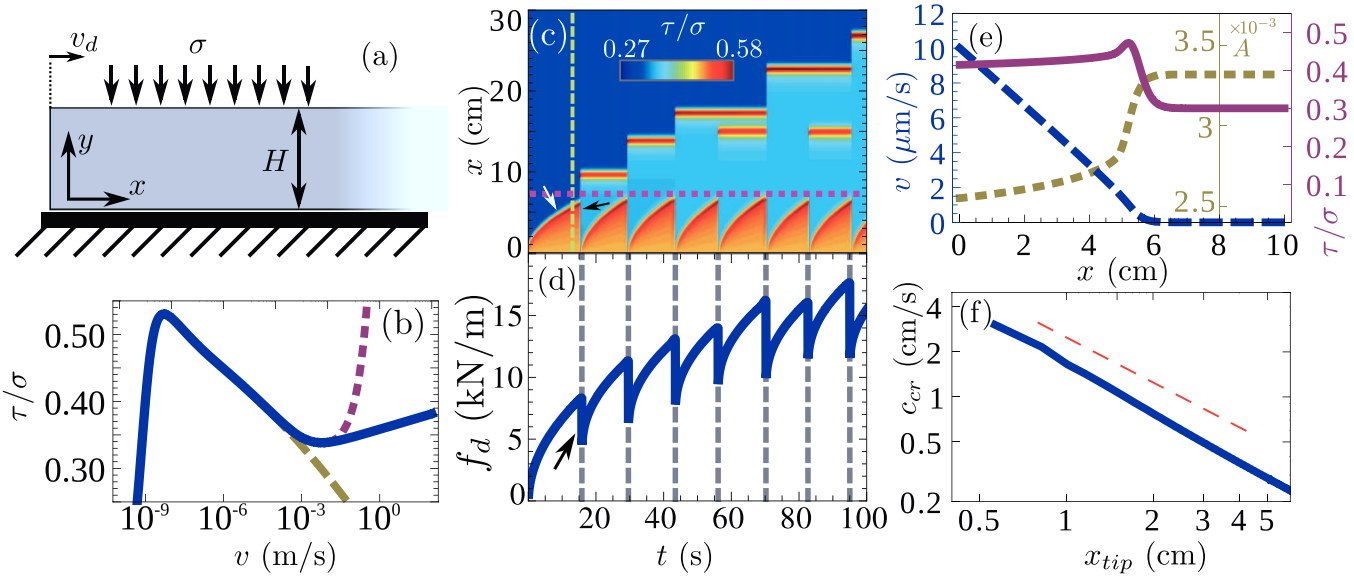

FIG. 1. (Color online) General phenomenology and creep patches. (a) The geometry and loading configuration studied here. (b) Steady-state sliding friction vs slip velocity v (solid blue line). The dashed yellow line shows steady friction which is purely velocity-weakening. The dotted purple line shows stronger-than-logarithmic (linear) strengthening. See text for details. (c) Spatiotemporal evolution of $\tau(x,t)/\sigma$. The blue regions correspond to the background stress $\tau = 300$ kPa. (d) The tangential force per unit width $f_d(t)$. (e) Example of $v(x,t)$, $\tau(x,t)/\sigma$, and $A(x,t)$ of the creep patch at the time marked by a vertical dashed line in panel (c). (f) $c_{\rm cr}$ vs $x_{\rm tip}$ in log scale. The dashed line shows a slope of -1.

sliding friction curve [obtained by setting to zero the time derivatives in Eqs. (1)] is shown in Fig. 1(b) (solid line). The curve has a peak at extremely small slip velocities (related to v_0), which we believe to be a generic feature of friction, though it is of no significance here [45,46]. Moreover, the curve exhibits a crossover from velocity-weakening behavior to velocity-strengthening behavior (at v_m, here a few mm/s). This feature has been experimentally observed in many materials [47] and plays an important role below.

The initial conditions for the friction variables are representative of laboratory experiments, $\tau^{\rm el}(x,t=0) = 300$ kPa and $\phi(t=0) = 1$ s [28,29]. The existence of an initial stress distribution $\tau^{\rm el}(x,t=0)$ was shown to be a generic feature of frictional systems [28], and—as also shown below—to affect the subsequent failure dynamics. Additional shear stresses are inhomogeneously applied to the system through moving its trailing edge at $x = 0$ at a constant speed $v_d = 10$ μm/s, again typical to laboratory experiments [25,28,42]. The resulting applied tangential force per unit thickness $f_d(t)$ is tracked.

Numerical results. We first characterize the phenomenology of the model through numerical simulations (the spatially discretized system of equations was integrated in time using a standard ordinary differential equation solver in MATHEMATICA), a typical example of which is shown in Figs. 1(c) and 1(d). $f_d(t)$ is shown in Fig. 1(d) to continuously curve (after a short quasilinear increase) and to experience sharp, discrete-like drops [25,48].

To better characterize this behavior, we focus on the corresponding spatiotemporal dynamics of $\tau(x,t)/\sigma$ in the color map in Fig. 1(c) [sharing the same time axis with Fig. 1(d)]. The continuous curving of $f_d(t)$ corresponds to the propagation of a *creep patch* that extends from $x = 0$ into the interface and decelerates continuously (marked with a white arrow). When the creep patch reaches a certain size (marked by the horizontal dashed line), at $t \simeq 16$ s, it loses stability, and a much faster rupture front emerges and propagates until it arrests at $x \simeq 10$ cm. The rupture front propagation, responsible for the drop in $f_d(t)$ (marked by the black arrows in both panels), appears as a vertical line in the color map because of the enormous variation in the time scales involved, though its velocity is finite (see below). A movie of the spatiotemporal dynamics is available in the Supplemental Material [44].

When the rupture front arrests it leaves behind it an inhomogeneous stress distribution with a rather localized peak at the arrest location, which can be interpreted as the front tip. At the same time, another creep patch initiates and extends from the trailing edge until it loses stability at the *same size* as before and again a much faster rupture front propagates, collides with the previously arrested front tip, and continues to propagate until it arrests deeper inside the interface (this time at $x \simeq 14$ cm). This process repeats itself almost periodically, though some heterogeneity appears (not discussed here).

Creep patches. A closer look at the creep patch is shown in Fig. 1(e), which presents a snapshot of the spatial distribution of the fields $v(x,t)$, $\tau(x,t)/\sigma$, and $A(x,t)$ at t corresponding to the vertical dashed line in Fig. 1(c) (prior to the instability). All fields relax to their spatially homogeneous background values at the same point ($x \simeq 6$ cm for that snapshot), which is the boundary between slipping and nonslipping regions, denoted by $x_{\rm tip}$. To compute the creep patch velocity $c_{\rm cr} \equiv \dot{x}_{\rm tip}$, we assume that its dynamics are quasistatic and therefore neglect the inertial and viscous terms in Eq. (2). We further replace $\tau^{\rm el}$ by its fixed point to obtain $\bar{G}H\partial_{xx}u \simeq \mu_0 DA(\phi)/h$.

Transforming to a comoving coordinate $\xi = x - c_{\rm cr}t$ and estimating $\partial_x v \simeq v_d/x_{\rm tip}$, the above relation yields

$$c_{\rm cr} \simeq v_d \frac{\bar{G}Hh}{\mu_0 DA(\phi_{\rm tip})} \frac{1}{x_{\rm tip}}, \tag{3}$$

where $\phi_{\rm tip}$ is an estimation of ϕ at the tip. This result shows that the creep patch propagation is directly driven by the loading as $c_{\rm cr}$ is proportional to v_d [48]. Possibly related loading-rate-dependent creep patches were observed in [49]. Moreover, Eq. (3) predicts that the creep patch decelerates as it extends, its propagation velocity being inversely proportional to its size, which is a property of the side-loading configuration. This prediction is verified in Fig. 1(f). Finally, we note that while $c_{\rm cr}$ is significantly larger than the loading rate $v_d = 10\ \mu$m/s—in the cm/s range for our parameters here [cf. Fig. 1(f)]—it is still orders of magnitude slower than "slow" rupture [23,27,28] and should not be confused with it.

Instability of creep patches (rupture nucleation). Rapid slip nucleation (instability) at a critical size L_c has been extensively discussed previously [2,22,49–51] and is understood to result from a competition between frictional weakening and the variation of the effective bulk stiffness with the patch size. The present framework allows us to analyze the instability very cleanly and carefully test the analytic predictions.

To analyze the stability of the creep patch we first note that its slip velocity is small and belongs to the weakening branch of the steady friction curve shown in Fig. 1(b). Therefore, we rewrite Eq. (2) as $\bar{G}H\partial_{xx}u \simeq \tau \simeq \tau_{\rm ss}(v)$, where $\tau_{\rm ss}(v)$ is the velocity-weakening steady-state friction branch. We then introduce a displacement perturbation of the form $\delta u(x,t) = \delta u_0\, e^{ikx+\lambda t}$ in the above relation to obtain

$$k^2\bar{G}H\delta u \simeq |\partial\tau_{\rm ss}/\partial v|\,\delta v \simeq \lambda\,|\partial\tau_{\rm ss}/\partial v|\,\delta u, \qquad (4)$$

resulting in an instability spectrum $\lambda \sim k^2$, in which larger k-vector modes grow faster. The spectrum is regularized by the intrinsic friction time scale, $\lambda \simeq v/D$, which yields for the most unstable mode $k_c = 2\pi/L_c$ the following critical wavelength:

$$L_c \simeq 2\pi\sqrt{\frac{\bar{G}HD}{|\partial\tau_{ss}/\partial\ln v|}}. \qquad (5)$$

The analysis above predicts that creep patches undergo a linear instability when $x_{\rm tip} = L_c$, given in Eq. (5). This prediction is tested in detail in Fig. 2. The dependence (and independence) of L_c on various parameters in Eq. (5) is verified in Fig. 2(a). A snapshot of the velocity distribution during the initial growth of the instability is shown in Fig. 2(b). Superimposing $\cos(2\pi x/L_c)$ (i.e., the real part of e^{ik_cx}) on it yields excellent agreement (see figure for details), which demonstrates that this is indeed a linear instability. Finally, our linear stability analysis predicts that $\lambda \simeq v_d/D \simeq (50\ {\rm ms})^{-1}$, where v_d (the loading rate) is the maximal slip velocity in the creep patch [cf. Fig. 1(e)]. Figure 2(c) shows that the instability amplitude initially grows exponentially with a typical time of 26 ms, in favorable agreement with the predictions. A movie of the instability is available in the Supplemental Material [44].

To conclude the discussion of the instability we note that since $|\partial\tau_{\rm ss}/\partial\ln v|$ in the weakening regime is v-independent, L_c in Eq. (5) is v-independent as well. Moreover, L_c is independent of the stress state as is clearly demonstrated by the horizontal dashed line in Fig. 1(c) (see below additional results concerning this point). The connection between Eq. (5) and available results in 2D is discussed in the Supplemental Material [44].

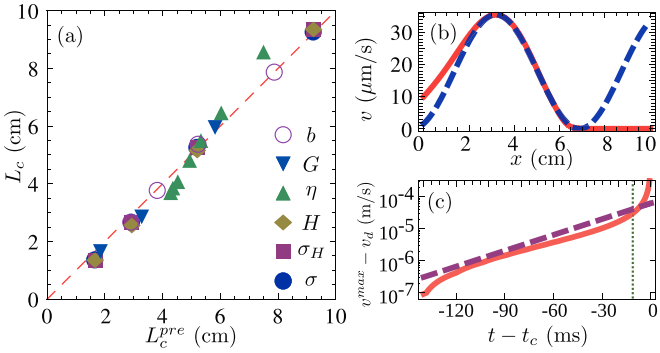

FIG. 2. (Color online) Onset of instability. (a) The measured L_c (in the simulation) vs the prediction [Eq. (5)]. The parameters varied are shown in the legend (the dashed red line has a slope 1 and goes through the origin). (b) Snapshot of $v(x,t)$ near the onset of instability [solid red line; t corresponds to the vertical line in (c)]. $1+\cos(2\pi x/L_c)$, x-shifted and amplitude-scaled, is superimposed (dashed blue line). (c) The instability grows exponentially with time scale of 26 ms. $v^{\rm max}(t)$ is the instantaneous spatial maximum of $v(x,t)$ and t_c is defined in Fig. 3.

Outcome of instability (rupture fronts). After an initial exponential growth, the instability enters the nonlinear regime, characterized by a steadily propagating rupture front that is excited for a few tens of μs and is accompanied by significant, much faster slip (see Fig. 3). What determines the rupture front properties?

In [37] it was conjectured that transient rupture fronts propagating under spatially inhomogeneous stress conditions might be short-lived excitations of steady-state rupture fronts propagating under homogeneous stress conditions. The latter exist only in the presence of a nonmonotonic steady friction law [cf. Fig. 2(b)] and span a continuous spectrum of propagation velocities with a finite minimal value [37]. To

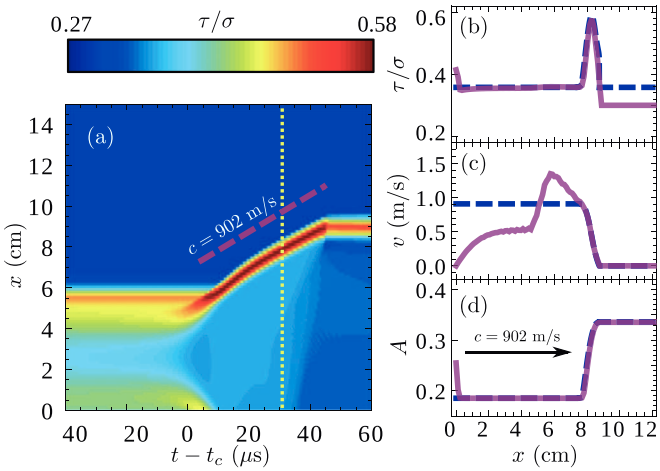

FIG. 3. (Color online) Outcome of instability. (a) High temporal resolution of the dynamics of $\tau(x,t)/\sigma$ during instability (see movie in the Supplemental Material [44]). t_c is defined as the zero of the time axis here (roughly at the onset of nonlinearity). (b)–(d) A snapshot of the field distributions during rupture propagation at a time corresponding to the vertical dashed line in panel (a) (solid purple lines). The propagation velocity is $c = 902$ m/s. The dashed blue lines are described in the text.

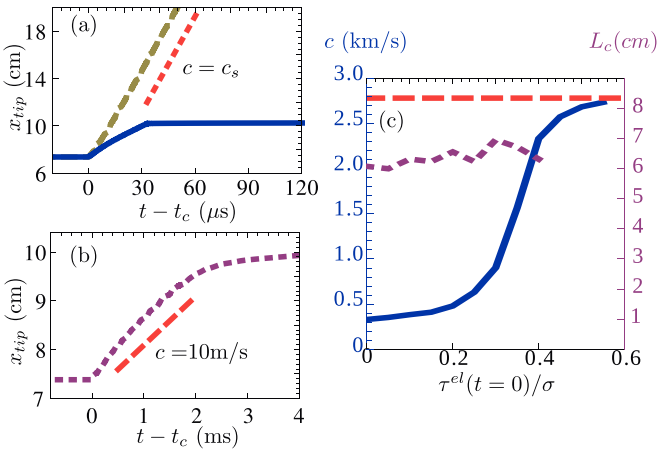

FIG. 4. (Color online) Effect of velocity-strengthening and initial stress. (a) The front location $x_{\rm tip}$ during the first rupture event for logarithmic velocity-strengthening (solid blue line) and for purely velocity-weakening friction (dashed yellow line). The dotted red line corresponds to the elastic wave speed. (b) $x_{\rm tip}$ for linear strengthening. Note the dramatic change in the time scale as compared to panel (a). The dashed red line corresponds to $c = 10$ m/s. (c) L_c (dotted purple line, right y axis) and c (solid blue line, left y axis) vs $\tau^{\rm el}(t = 0)/\sigma$. The dashed horizontal line is the elastic wave speed.

test this idea, we choose a steady-state-front solution whose propagation velocity c is the same as in Fig. 3 ($c = 902$ m/s, which is 32% of the elastic wave-speed $c_s = \sqrt{\bar{G}/\rho} = 2783$ m/s) and which penetrates an interface of the same "age" (i.e., $\phi = 17.4$ s). When superimposing it on the transient front [solid purple lines in Figs. 3(b)–3(d)], we observe that all fields exhibit reasonable agreement, including the detailed distribution of $\tau(x,t)/\sigma$ and the typical slip velocity behind the front, lending support to our conjecture. Currently we cannot theoretically predict the selection (i.e., why this particular c was selected), which might be a "soft selection" due to the (weak) logarithmic velocity-strengthening.

To further test this conjecture, and explore the role played by the velocity-strengthening branch in general, we study two variants of our model, one in which friction is purely velocity-weakening [cf. the dashed yellow line in Fig. 1(b)] and one in which velocity-strengthening is linear in v [cf. the dotted purple line in Fig. 1(b)] [26,35,36,47]. In the former case, rupture propagates at the elastic wave speed c_s, penetrates much deeper into the interface, and results in a much larger stress drop [see Fig. 4(a)]. In the latter case, rupture propagates at a much slower velocity $c \simeq 10$ m/s $\ll c_s$ [see Fig. 4(b)], comparable to the smallest velocity member in the spectrum of steady-state-front solutions [37,48]. We identify it as "slow" rupture [23,27]. These results clearly indicate that the existence and functional form of the velocity-strengthening branch significantly affect rupture dynamics. This seems to be directly related to the new experimental observations of [52] and might also explain why models that do not include velocity-strengthening friction typically feature only very fast rupture events [10].

Finally, we study the effect of the initial stress level on the onset of instability and the resulting rupture (for logarithmic velocity-strengthening). Figure 4(c) shows that a prestress $\tau^{\rm el}(t = 0)$ significantly affects the rupture velocity (and hence the event's magnitude), while L_c is almost unaffected [note that at $t = 0$, $\tau^{el}(t=0)$ is balanced by $\partial_{xx}u$ in Eq. (2)]. In a geophysical context, this result seems to agree with the statement that "the size of an event is determined by the conditions on the fault segments the event is propagating into rather than by the nucleation process itself" [2]. In addition, we note that the variation of the rupture propagation velocity with the prestress level resembles the recent experimental results of [28] (cf. Fig. 3 therein).

The results described in this communication were obtained in the quasi-1D limit of small H. The scaling structure of the corresponding 2D results may be obtained through the procedure described in the Supplemental Material [44]. While we suspect that the qualitative nature of our results remains unchanged in higher dimensions, quantitative aspects should be carefully explored in future research.

Concluding remarks. In conclusion, we showed that creep patches extending at frictional interfaces undergo a linear instability at a critical nucleation size that is nearly independent of the stress state and the presence of velocity-strengthening friction. The post-instability nonlinear evolution results in rapid slip mediated by rupture fronts whose properties do depend on the stress state, the presence of velocity-strengthening friction, and its functional form. In particular, the absence of velocity-strengthening friction facilitates large slip events that propagate at velocities approaching the elastic wave speed and its presence gives rise to significantly smaller and slower slip events. Finally, we related transiently propagating rupture fronts to homogeneously driven steady-state fronts [37] and showed that initial stresses systematically affect the rupture dynamics. These robust results (i.e., parameter-insensitive) may have significant implications for our understanding of interfacial failure and are currently extended to 2D.

Acknowledgments. E.B. acknowledges support of the James S. McDonnell Foundation, the Minerva Foundation, the Harold Perlman Family Foundation, and the William Z. and Eda Bess Novick Young Scientist Fund. E.A.B. acknowledges support of the Erna and Jacob Michael visiting professorship funds at Weizmann Institute of Science.

[1] C. Marone, Annu. Rev. Earth Planet. Sci. **26**, 643 (1998).
[2] N. Lapusta, J. R. Rice, Y. Ben-Zion, and G. Zheng, J. Geophys. Res. **105**, 23765 (2000).
[3] N. Lapusta and J. R. Rice, J. Geophys. Res. **108**, 2205 (2003).
[4] A. M. Rubin and J.-P. Ampuero, J. Geophys. Res. **110**, B11312 (2005).
[5] T. Baumberger and C. Caroli, Adv. in Phys. **55**, 279 (2006).
[6] J.-P. Ampuero and A. M. Rubin, J. Geophys. Res. **113**, B01302 (2008).
[7] Y. Ben-Zion, Rev. Geophys. **46**, RG4006 (2008).
[8] O. M. Braun, I. Barel, and M. Urbakh, Phys. Rev. Lett. **103**, 194301 (2009).

[9] R. Capozza and M. Urbakh, Phys. Rev. B **86**, 085430 (2012).
[10] Z. Shi, A. Needleman, and Y. Ben-Zion, Int. J. Fract. **162**, 51 (2010).
[11] A. Bizzarri, Geophys. Res. Lett. **37**, L18307 (2010).
[12] J. Trømborg, J. Scheibert, D. S. Amundsen, K. Thøgersen, and A. Malthe-Sørenssen, Phys. Rev. Lett. **107**, 074301 (2011).
[13] D. S. Amundsen, J. Scheibert, K. Thøgersen, J. Trømborg, and A. Malthe-Sørenssen, Tribol. Lett. **45**, 357 (2012).
[14] D. S. Kammer, V. A. Yastrebov, P. Spijker, and J. F. Molinari, Tribol. Lett. **48**, 27 (2012).
[15] M. Otsuki and H. Matsukawa, Sci. Rep. **3**, 1586 (2013).
[16] R. Capozza, I. Barel, and M. Urbakh, Sci. Rep. **3**, 1896 (2013).
[17] M. Cocco and A. Bizzarri, Geophys. Res. Lett. **29**, 1516 (2002).
[18] A. Vanossi, N. Manini, M. Urbakh, S. Zapperi, and E. Tosatti, Rev. Mod. Phys. **85**, 529 (2013).
[19] B. N. J. Persson, *Sliding Friction: Physical Principles and Applications* (Springer-Verlag, New York, 2000).
[20] B. Lorenz and B. N. J. Persson, J. Phys. Condens. Matter **24**, 225008 (2012).
[21] P. Berthoud, T. Baumberger, C. G'Sell, and J.-M. Hiver, Phys. Rev. B **59**, 14313 (1999).
[22] M. Ohnaka, Pure Appl. Geophys. **157**, 2259 (2000).
[23] S. M. Rubinstein, G. Cohen, and J. Fineberg, Nature (London) **430**, 1005 (2004).
[24] M. Nakatani and C. H. Scholz, J. Geophys. Res. **111**, B12208 (2006).
[25] S. M. Rubinstein, G. Cohen, and J. Fineberg, Phys. Rev. Lett. **98**, 226103 (2007).
[26] Z. Reches and D. A. Lockner, Nature (London) **467**, 452 (2010).
[27] S. Nielsen, J. Taddeucci, and S. Vinciguerra, Geophys. J. Int. **180**, 697 (2010).
[28] O. Ben-David, G. Cohen, and J. Fineberg, Science **330**, 211 (2010).
[29] O. Ben-David, S. M. Rubinstein, and J. Fineberg, Nature (London) **463**, 76 (2010).
[30] K. Nagata, M. Nakatani, and S. Yoshida, J. Geophys. Res. **117**, B02314 (2012).
[31] J. C. Chang, D. A. Lockner, and Z. Reches, Science **338**, 101 (2012).
[32] O. Ben-David and J. Fineberg, Phys. Rev. Lett. **106**, 254301 (2011).
[33] J. H. Dieterich, Pure Appl. Geophys. **116**, 790 (1978).
[34] A. Ruina, J. Geophys. Res. **88**, 10359 (1983).
[35] J. D. Weeks, J. Geophys. Res. **98**, 17637 (1993).
[36] F. Heslot, T. Baumberger, B. Perrin, B. Caroli, and C. Caroli, Phys. Rev. E **49**, 4973 (1994).
[37] Y. Bar Sinai, E. A. Brener, and E. Bouchbinder, Geophys. Res. Lett. **39**, L03308 (2012).
[38] T. Cao and K. Aki, Pure Appl. Geophys. **124**, 487 (1986).
[39] C. G. Sammis and J. R. Rice, Bull. Seismol. Soc. Am. **91**, 532 (2001).
[40] A. H. Kohli, D. L. Goldsby, G. Hirth, and T. Tullis, J. Geophys. Res. **116**, B03202 (2011).
[41] F. Bowden and D. Tabor, *The Friction and Lubrication of Solids* (Oxford University Press, London, 2001).
[42] T. Baumberger, P. Berthoud, and C. Caroli, Phys. Rev. B **60**, 3928 (1999).
[43] J. R. Rice, N. Lapusta, and K. Ranjith, J. Mech. Phys. Solids **49**, 1865 (2001).
[44] See Supplemental Material at http://link.aps.org/supplemental/10.1103/PhysRevE.88.060403 for additional theoretical background, parameters values and movies.
[45] Y. Estrin and Y. Bréchet, Pure Appl. Geophys. **147**, 745 (1996).
[46] T. Shimamoto, Science **231**, 711 (1986).
[47] Y. Bar-Sinai, R. Spatschek, E. A. Brener, and E. Bouchbinder, arXiv:1308.1420.
[48] E. Bouchbinder, E. A. Brener, I. Barel, and M. Urbakh, Phys. Rev. Lett. **107**, 235501 (2011).
[49] M. Ohnaka and L. F. Shen, J. Geophys. Res.: Solid Earth **104**, 817 (1999).
[50] J. R. Rice and A. Ruina, J. Appl. Mech. **50**, 343 (1983).
[51] J. H. Dieterich, Tectonophysics **211**, 115 (1992).
[52] B. M. Kaproth and C. Marone, Science **341**, 1229 (2013).